Multi-species PLIF study of the structures of turbulent premixed methane/air jet flames in the flamelet and thin-reaction zones regimes

Rosell, Joakim; Bai, Xue Song; Sjöholm, Johan; Zhou, Bo; Li, Zheming; Wang, Zhenkan; Pettersson, Per; Li, Zhongshan; Richter, Mattias; Alden, Marcus

Published in:
Combustion and Flame

DOI:
10.1016/j.combustflame.2017.04.003

2017

Document Version:
Peer reviewed version (aka post-print)

Multi-species PLIF study of the structures of turbulent premixed methane/air jet flames in the flamelet and thin-reaction zones regimes

Joakim Rosell[1], Xue-Song Bai[2], Johan Sjoholm[1], Bo Zhou[1], Zheming Li[1], Zhenkan Wang[1], Per Pettersson[1], Zhongshan Li[1], Mattias Richter[1], Marcus Alden[1]

[1]Division of Combustion Physics, Lund University, 221 00 Lund Sweden

[2]Division of Fluid Mechanics, Lund University, 221 00 Lund Sweden

Abstract

Simultaneously planar laser-induced fluorescence (PLIF) measurements of OH, CH, CH_2O and toluene are carried out to investigate the structures of turbulent premixed methane/air jet flames in the flamelet regime and the thin-reaction zones regime. A premixed flame jet burner of an inner diameter of 1.5 mm is employed. Stoichiometric methane/air mixtures introduced as a jet are ignited and stabilized in a hot co-flow generated by a coaxial porous plug pilot flame surrounding the jet. The Reynolds number for the studied jet ranges from 960 to 11500 with the characteristic Karlovitz number ranging from 1 to 60. The focus of this study is on the characterization of the structures and turbulent burning velocity of premixed flames in the flamelet and the thin-reaction zones regimes. The preheat zone is analyzed using the CH_2O and toluene PLIF fields, whereas the reaction zone is analyzed using the CH and OH PLIF fields. Laser Doppler Anemometer (LDA) measurements are performed to characterize the turbulence field and it is noted that when the Reynolds/Karlovitz number increases a successive thickening of the preheat zone is observed, whereas the reaction zone, characterized by the CH layer maintains nearly the same thickness. The heat release zone, characterized by the combination of the OH and CH_2O PLIF fields, is

shown to nearly maintain the same thickness under the present experimental conditions. The flame surface wrinkle ratio is shown to be Reynolds number and Karlovitz number independent when the Reynolds number is high enough such that the smallest wrinkle scales reach to the length scales of the thin reaction layers. The global fuel consumption speed of the jet flame is analyzed using the toluene PLIF field and the OH PLIF field. A discrepancy in the two consumption velocities is found as the Karlovitz number increases. This is found to be a result of the broadening of the oxidation zone. These findings provide experimental support to the flamelet and thin-reaction zone regime hypotheses of turbulent premixed combustion.

Keywords: Multiple species simultaneous PLIF; turbulent premixed flames; Karlovitz number; flamelet regime; thin-reaction zone regime.

1. Introduction

Depending on the flame and the time and length scales of the turbulence, different regimes of turbulent premixed flames can be classified, e.g., laminar flamelet, thin-reaction zone, and distributed reaction zone regimes [1-3]. Flames in the laminar flamelet regime have been studied comprehensively in the past [4-7]; the reaction zones in the flamelet regime are thinner than the length scale of Kolmogorov eddies and the structure of the flame is essentially similar to those of laminar flames. Driscoll presented a comprehensive review of the structures of turbulent premixed flames in the flamelet regime [4]. Flames in the thin-reaction zone regime and distributed reactions zone regime are not as well investigated. Theory based on asymptotic analysis of laminar premixed flames predicted that in the thin-reaction zone regime, the structure of the fuel-consumption layer in hydrocarbon/air premixed flames is similar to that in laminar flames [3, 8];

however, the preheat zone and the oxidation layer of the flames (where the combustion intermediates such as CO and H_2 are oxidized) could be thickened by small turbulence eddies.

Several direct numerical simulations (DNS) of premixed flames appear to support the thin reaction regime theory. The DNS study of Poinsot et al. [9] indicated that the flamelet model could be valid beyond the flamelet regime, at higher turbulence intensity than the Klimov-Williams limit (at which the Kolmogorov time is on the order of the flame time). The work of Poludnenko and Oran [10], which considered the case of stoichiometric H_2-air flame in the thin reaction regime using a simplified chemistry, showed that the turbulent cascade failed to penetrate the internal flame structure, and thus the action of small-scale turbulence was suppressed throughout most of the flame. It was speculated that any substantial flame broadening by the action of turbulence could not be expected in all subsonic regimes. The DNS study of Shim et al. [11], which considered H_2-air freely propagating premixed flame in homogeneous isotropic turbulence using detailed chemistry, showed that in the thin reaction zone coherent fine scale eddies could be frequently observed behind the flame front and the heat release rate was highly fluctuating even at the low temperature region. In the unburned side HO_2 fingering can be observed suggesting a strong eddy transport between the preheat zone and the unburned side of the mixture. DNS study of Sakaran et al. [12] on lean methane/air premixed flames in a slot burner Bunsen configuration showed that in the thin reaction zone regime the preheat zone is broadened but the heat release region remains the same thickness when increasing the turbulence intensity. Aspdan et al. [13] showed similar results in their recent DNS of premixed methane/air flames in a homogeneous isotropic turbulence configuration.

So far, experiments on the thin reaction regime have been fairly limited and the results appear to be controversy. Chen and Bilger [14-17] carried out joint measurements of temperature using Rayleigh scattering and OH mole fraction using PLIF in turbulent premixed flames of natural-gas/air and hydrogen/air in pilot-stabilized Bunsen burner in the thin-reaction regime. Multiple

joint image pairs showed distortion and folding of the preheat zone at high turbulence intensities and they proposed a new regime of "flame fronts with complex strain". De Goey et al. [7] performed planar laser-induced fluorescence (PLIF) imaging of OH radicals and Rayleigh scattering imaging of temperature and one-dimensional numerical study of the structures of turbulent methane/air premixed flames in the thin-reaction zone regime. They found that the preheat zone (defined as the temperature ranges from the unburned temperature, 298K, to the temperature of 340K) could be broadened; the reaction zone (defined at the maximal temperature gradient) could, however, become even thinner in the thin-reaction zone regime, depending on the equivalence ratio. This was found to be an effect of flame stretch. Kortschik et al. [18] reported similar findings of turbulent premixed methane/air flames in the thin-reaction zone regime. Dunn et al. [19, 20] reported detailed measurement of multiple species and temperature as well as velocity of methane/air premixed flames in a piloted premixed jet burner with a wide range of jet velocities, covering the thin reaction regime as well as the distributed reaction zone regime. They found that the thickness of the reaction (marked by the temperature gradient) increases with increasing jet velocity, which is contrary to the results in reaction zone behavior reported in De Goey et al. [7]. Yuan and Gülder [21] performed particle imaging velocimetry (PIV) of velocity and Rayleigh scattering measurements of temperature of turbulent methane/air Bunsen flames stabilized in a hot co-flow and determined the mean thickness of the preheat zone and reaction zone using the temperature profiles. They found that the thickness of the reaction zone was in the range of 0.7 – 0.8 mm and the preheat zone was in the range of 0.8 – 1 mm for the studied conditions that ranges from laminar flamelet regime to thin-reaction zone regime.

Most of the above-discussed experimental studies were limited to study only a few scalars, e.g., OH and temperature, and mostly these scalars were not simultaneously measured. Experimental quantification of the structures of turbulent premixed flames requires simultaneous spa-

tially resolved measurements of key species in the flames, e.g., the OH and CH_2O. A multiplication of these two fields can be used as a measure of the heat release layer in laminar flamelets [22, 23]. Recently, Sjöholm et al. [24] demonstrated simultaneous PLIF imaging of CH, OH, CH_2O and toluene (as fuel tracer) applied to turbulent premixed jet flames [25], which shows the possibility of identifying the structures of turbulent flames, e.g. the unburned region, the preheat zone, the reaction zone and the post-flame zone. Similar techniques, with pairwise recording of relevant species, have been used to study turbulent premixed flames in the thin reaction zone and distributed reaction zones regime [26-29]. Despite the large-scale experimental setup and comprehensive implementation, such as; laser alignment, accurate synchronization, laser sheet overlapping, pixel-to-pixel correction, interferences suppressions etc., simultaneous PLIF visualization are preferred as more phenomenological conclusions on the combustion processes can be scrutinized.

In this paper, we employ simultaneous, single shot PLIF of four species (OH, CH, CH_2O, and toluene) to study the flame structures of turbulent premixed flames in the flamelet regime and the thin-reaction zone regime. The unburned fuel zone is characterized using toluene PLIF [24]; the preheat zone is identified using CH_2O PLIF [25] or the overlap of CH_2O PLIF field and toluene PLIF field; the inner layer (fuel consumption zone) is characterized using CH PLIF, and the heat release zone by the overlap of the CH_2O PLIF field and OH PLIF field [22]. The studied flames are stoichiometric methane/air premixed jet flames stabilized in a hot co-flow generated by a porous plug burner surrounding the jet nozzle. The turbulent flow field along the flame height is characterized by laser Doppler Anemometer (LDA) applied at different height above the burner (HAB) and at several radial positions. This work is focused on the thin-reaction zone regime of turbulent premixed flames, in particular the structures of the preheat zone, the inner layer of the flame and the heat release layer.

2. Experimental Method

2.1 Burner and experimental conditions

The burner is a McKenna type with a porous plug of 61 mm in diameter and an coaxial central tube with an inner diameter of 1.5 mm. Figure 1 shows a schematic of the burner (to the right). Stoichiometric methane/air mixture is supplied through the jet burner at different velocities. The bulk flow velocity at the jet exit, U_0, ranges from 10 m/s to 120 m/s. The porous plug burner provides a steady pilot stoichiometric methane/air flame with a velocity 0.4 m/s of the unburned mixture, which was used to stabilize the jet flame. Table 1 lists the experimental cases and the corresponding conditions. The Reynolds number based on the inner diameter of the jet and the bulk flow velocity at the jet exit ranges from 960 to 11500. Flame F0 (U_0 = 10 m/s) is at a laminar flow condition, whereas Flame F1 (U_0 = 30 m/s) is a quasi-laminar flow (with some unsteady modes), and flames F2, F3 and F4 are at turbulent flow conditions. Both flames F3 and F4 are fully developed turbulent flows, which is indicated by the self-similar flow fields to be discussed in the Results section, where the LDA flow field measurements will be presented in more detail.

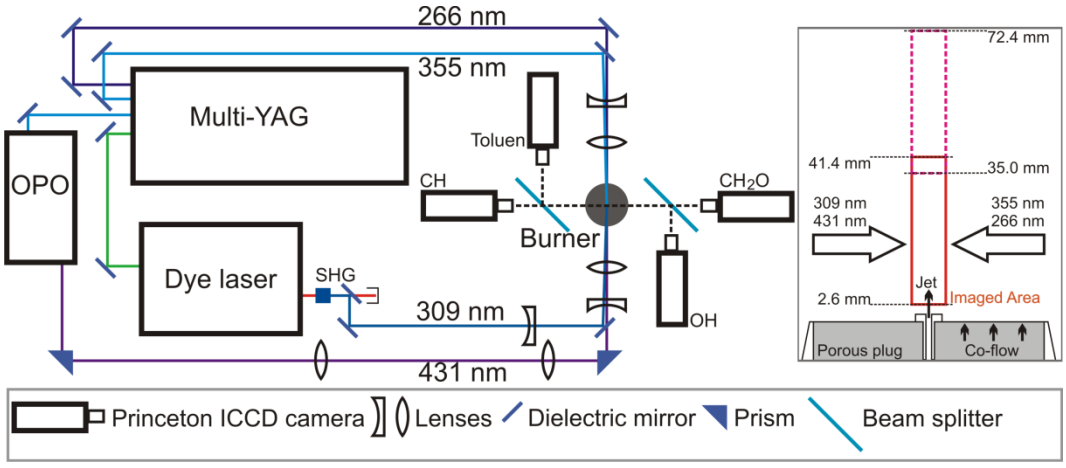

Figure 1. Setup of the multi-species PLIF system (left), and illustration of the burner (right).

Table 1. Experimental conditions and key parameters. Velocity of the co-flow fuel/air mixture: U_{coflow}=0.4 m/s; equivalence ratio of the mixture from the jet and the co-flow: 1.0; initial temperature of mixture from the jet and the co-flow: 298K; pressure: 1 atm; burning velocity (S_L) and thickness (δ_L) of unstretched adiabatic flame under the fuel/air mixture condition of the experiment: S_L=37.5 cm/s; δ_L=0.44 mm. The data in Table 1 is taken at the location of peak turbulence rms velocity, which is about x/d=40.

Flames	F0	F1	F2	F3	F4
U_0 [m/s]	10	30	60	90	120
Re_{jet}	960	2900	5700	8600	11500
u'/S_L	-	-	22	29	38
ℓ_0/δ_L	-	-	19	15	15
Ka	-	-	25	40	60
Re_t	-	-	400	425	570
ℓ_k [μm]	-	-	91	69	56

2.2 Multi-species PLIF setup

The methane/air flow in the central jet is seeded with ~2 % toluene as a fuel tracer. Sjöholm et al. [24] presented a numerical simulation of a laminar methane/air planar freely propagating flame with a 2 % toluene addition to methane. It was shown that with this amount of toluene added to methane the species (except methane) distributions across the flame are not significantly affected. A 1.3 % difference in the adiabatic unstretched laminar burning velocity was predicted. The profiles of methane and toluene are similar, although a slightly earlier consumption of toluene is noticeable, due to differences in reaction paths and molecular diffusivity. In this study the numerical simulation reported in Sjoholm et al. [24] is extended to a counter flow (unburned mixture to

unburned gas) configuration to study the structure of the flames under strain rates of 50 s^{-1} and 1000 s^{-1}. It is shown that under strained conditions the toluene layer and the methane layer are still satisfactorily coincident with each other, which confirms the validity of using toluene as a PLIF tracer for the fuel.

The multi-species PLIF setup has been described in Sjöholm et al. [24]. Here, a brief summary of the laser systems is given referring to Figure 1. Four separate Nd:YAG lasers in the Multi-YAG system [30, 31] provided four separate output beams with different wavelength. The first laser emitted 266 nm to excite the fuel-tracer toluene and the second laser emitted 355 nm to excite formaldehyde (CH_2O). These two beams were spatially overlapped before the sheet optics, which consisted of a -100 mm cylindrical and a +500 mm spherical lens. The sheet created was then cropped to a height of 40 mm.

The third laser from the Multi-YAG system also emitted 355 nm and pumped a mid-band optical parametric oscillator (OPO) [32] tuned to 431 nm for CH excitation. Due to low concentrations of CH in most combustion processes the fluorescence signal of CH is generally low.

The fourth laser emitted 532 nm and pumped a Sirah Cobra-Stretch dye laser, after frequency doubling the output beam was set to 309 nm, exciting OH. The selection of 309 nm, instead of 284 nm, is to avoid cross talk with toluene. The sheet-optics for these two beams was made up with a -40 mm cylindrical and a +300 mm spherical lens.

Four separate intensified CCD detectors were used, three PI-MAX II cameras (resolution: 1024 x 1024) and one PI-MAX I (resolution 512 x 512). A summary of optical parameters and filters are shown in Table 2.

Table 2. Key parameters of the PLIF setup.

Species	**Toluene**	**CH_2O**	**CH**	**OH**
Camera pixels	PI-MAX I 512 x 512	PI-MAX II 1024 x 1024	PI-MAX II 1024 x 1024	PI-MAX II 1024 x 1024
Beam splitter efficiency	R ~99 % 250 – 290 nm	T > 90 % 400 – 750 nm	T ~92 % @ 431 nm	R >99.9 % 287 – 335 nm
Lens	UV B. Halle lens $f_{\#}$ = 2, f = 100 mm	Nikkor, $f_{\#}$ = 2.5, f = 105 mm	Nikkor, $f_{\#}$ = 1.8, f = 105 mm	UV B. Halle lens $f_{\#}$ = 2, f = 100 mm
Spatial resolution	7.1 lines/mm	8.0 lines/mm	7.1 lines/mm	8.0 lines/mm
Optical Filter	Liquid filter, 12 mm thick, N,N-dimethylformamide	GG 385 and SP 500 $T_{total\ max}$ ~70 %	No filter (BK7 lens)	Interference filter l_T = 310 nm ± 5 nm T_{max} = 15 %
Imaging delay	300 ns	200 ns	0 ns	100 ns
Laser wavelength	266 nm	355 nm	431 nm	309 nm
Laser Energy	40 mJ/pulse	90 mJ/pulse	70 mJ/pulse	10 mJ/pulse
Laser line width	1 cm^{-1}	1 cm^{-1}	4 cm^{-1}	0.2 cm^{-1}
Detected λ	275 – 290 nm	385 – 500 nm	431 ±10 nm	309 ±5 nm
SNR	22.6	68.2	26.6	15.3

To measure the full length of the flame, the burner height had to be adjusted to two positions relative to the laser and the detector systems that were kept fixed. The lower part of the flames was measured first and then the burner was lowered 35 mm and PLIF images of the upper part of the flames were recorded.

2.3 *LDA setup*

A two channel LDA system (Flow Explorer DPSS & BSA F80 processor unit; Dantec) was used for the measurements of the axial and radial velocity components and its fluctuations. Diode Pumped Solid State (DPSS) lasers were used to generate beams at 532 nm and 561 nm with average power of 300 mW each. Each beam was split into two beams, of which one beam for each wavelength was optically shifted with a fixed frequency of 80 MHz. This setup allows detection of velocities up to 380 m/s. The two pairs of beams, the shifted and the unshifted beam for each wavelength, were focused to intersect by a 310 mm lens. The two measurement volumes, created at the beam intersection point, were overlapping with the interference fringes of each color oriented perpendicular to each other. The Gaussian intensity distribution of the laser beams generates an ellipsoidal effective measurement volume, one for each color, about 80 (width) × 80 (height) × 700 (length) μm^3 in size. The bursts of Mie scattered light generated by seeding particles crossing the fringes (i.e. the signal), was collected in a back-scatter mode with the signal receiving optics incorporated in the LDA probe.

The main jet flow was seeded with 0.5 μm Al_2O_3 particles mixed with the main fuel stream before entering the burner. The co-flow emanating from the porous plug burner could not be seeded in the present setup. The influence of a non-uniform seeding, under similar flow conditions, was investigated by Dibble et al. [33] in both non-reacting (propane jet, bulk velocity 53 m/s) and in an non-premixed jet (H_2-Ar flame, bulk velocity 150 m/s) both in co-flowing air (of 9.2 m/s). From experiments where either only the jet was seeded or only the co-flow was seeded they found only minor influence of the non-uniform seeding on the axial velocity statistics (mean and rms). Radial profiles of the mean axial velocity and its fluctuations (rms) (at x/D > 30) showed, for both seeding approaches, very small difference on the centerline and a slightly larger difference with increasing radius. Based on these results obtained in a similar configuration as in

this study the centerline statistics presented here are believed to be unbiased whereas a bias towards the higher velocities and fluctuations in the jet is expected with increasing distance from the centerline.

At different points along the center axis of the jet, from 4 mm up to 120 mm HAB and with 3 mm interval, velocities were measured along with radial profiles at selected heights. The reproducibility of mean (U) and rms (u') velocities at the same spatial positions was, on average, 5 %, mainly accounting for the mismatch of spatial relocation. The fixed errors were expected to be significant near the jet exit where the velocity gradient was large. The total error near the jet exit was estimated to be about 20 % for the mean axial velocity and 15 % for the rms of the axial velocity fluctuations.

2.4. *Data post-processing*

Image registration, i.e. pixel-to-pixel correspondence, between the four detectors was conducted using grid images, providing final images with the size of 985 x 270 pixels (lower images) and 950 x 270 pixels (upper images). This represented a 10.6 mm wide imaged area extending from 2.6 mm to 41.4 mm above the jet nozzle for the lower part, and from 35.0 mm to 72.4 mm above the jet nozzle for the upper part. The ~10 % overlap of the imaged areas is illustrated in Figure 1.

Each image was background-subtracted where the background image was recorded with lasers active and a burning co-flow but the jet flow turned off. Hence, the OH images would represent OH contribution from the jet flow to the total OH distribution. Finally, to reduce noise, a Gaussian filter (FWHM = 3.5 pixels) was convoluted to the images [24], where FWHM denotes full-width at half maximum.

The following quantities were computed from the PLIF data: the thickness of the CH layer, the thickness of the CH_2O layer, the thickness of the overlap layer of CH_2O and OH, the thickness of the overlap layer of CH_2O and toluene, the mean reaction progress variable based on the OH and toluene fields, the flame surface density, the flame surface wrinkle ratio, and the overall fuel consumption velocity. In addition, to characterize the regime of the flames a characteristic non-dimensional number, the Karlovitz number, along the flame height was determined based on the LDA data and laminar flame data given in Table 1. The Karlovitz number was calculated based on Peters definition [3],

$$Ka = \frac{t_f}{t_k} = \frac{Re_t^{1/2}}{Da} = \left(\frac{u'}{S_L}\right)^{3/2} \left(\frac{\delta_L}{\ell_0}\right)^{1/2}, \quad (1)$$

where t_f and t_k and are respectively the time scale of the corresponding adiabatic unstretched laminar flame and the time scales of the Kolmogorov eddies. S_L and δ_L are the corresponding adiabatic unstretched laminar flame speed and the thickness of the laminar flame, respectively; ℓ_0 is the length scale of the energy-containing eddies (known as the integral length-scale); u' is the velocity scale of the large energy-containing eddies, taken here as the rms of the axial velocity fluctuation. Furthermore, the turbulent Reynolds number, Re_t, and the Damköhler number, Da, were defined as,

$$Re_t = \frac{u'\ell_0}{S_L\delta_L}, \quad (2)$$

$$Da = \frac{t_0}{t_f} = \frac{\ell_0 S_L}{u'\delta_L}. \quad (3)$$

Re_t was based on the large scale energy-containing eddies. LDA data provided the information of u' and ℓ_0, which were used to determine non-dimensional numbers Ka, Re_t, and Da.

Since only two-dimensional cross-section of the flames was captured in PLIF measurements the surface area of a given layer was reduced to the length of the edge of the layer. The flame surface density Σ at a position (x, y) was computed as Shepherd proposed [34],

$$\Sigma(x,y) = \frac{\sum_{i=1}^{N} L_i(x,y)}{N\Delta x \Delta y} \tag{4}$$

where $L_i(x,y)$ is the length of the layer edge in the i-th PLIF sample at the position (x, y) within the interval of $[x - \frac{\Delta x}{2}, x + \frac{\Delta x}{2}]$ and $[y - \frac{\Delta y}{2}, y + \frac{\Delta y}{2}]$. *N* is the number of samples used in computation.

Direct numerical simulation (DNS) study of statistically two-dimensional V-flame from a slot-burner showed that for a given flame the two-dimensional flame surface density was proportional to the three-dimensional flame surface density area, with the 2D surface density 35 % lower than the 3D one [35]. Several authors have proposed different ways of estimating the 3D flame surface density from the 2D experimental data, cf. Ref. [36] and references therein. For a Bunsen flame at three different turbulence intensities Zhang et al. [36] compared the results from these various estimations and found that the proportionality of 3D flame surface density to the 2D one varies with flame height. The difference between 2D and 3D flame surface is higher at high turbulence intensities. In the present study we show only the 2D results, which could be extended to 3D flame surface density used by the methods discussed in Ref. [36].

In addition to the flame surface density the flame surface wrinkle ratio $\sigma(x)$ is also a useful parameter to characterize the structure of premixed flames. The flame surface wrinkle ratio at a given flame height (*x*) was computed as follows,

$$\sigma(x) = \frac{\sum_{i=1}^{N} \sum_{j=1}^{M} L_{ij}(x)}{N\Delta x} \tag{5}$$

where $L_{ij}(x)$ is the length of the edge of the layer in the i-th PLIF sample at the flame height (x) within the interval of $[x - \frac{\Delta x}{2}, x + \frac{\Delta x}{2}]$, where $\Delta x = 5$ mm corresponds to 130 pixels. In case the flame was highly wrinkled there could be multiple flame edges detected in the interval; thus the total length of all edges was used to compute $\sigma(x)$. In Eq. (5), *M* is the total number of edges detected in the interval and index *j* denotes the j-th edge. The mean flame surface position can be determined using ensemble average of the flame edges. Denote the mean flame surface position as

$$y - f(x) = 0 \tag{6}$$

From which the total flame surface area can be determined,

$$A = 2\pi \int_0^{L_f} f(x)\sqrt{1 + (f'(x))^2}dx \tag{7}$$

where L_f is the height of the mean flame, $f(L_f) = 0$. The area averaged overall fuel consumption velocity was calculated using

$$S_c = \frac{1}{4}\pi d^2 U_0 / A \tag{8}$$

where *d* is the inner diameter of the jet.

The mean reaction progress variables, $<c_{OH}>$ and $<c_F>$, were calculated based on the OH and toluene fields to characterize the oxidation layer of combustion intermediates such as CO and H_2, and the fuel consumption layer. To get <c> a binary mask, with the threshold value of 5 % of the peak PLIF intensity for OH and 35 % of the peak intensity for toluene, were applied to all images and then averaged. The threshold values for OH and Toluene were carefully chosen to circumvent the noise in order to get monotonic images. This threshold method was compared with the maximum gradient method applied to calculate the flame surface wrinkle ratio (Eq.5). As the gradient of going from unburned gas to burned gas is steep, no considerable difference was found when

using a threshold value or maximum gradient. The difference in flame positions between using the maximum gradient and using a threshold value at 5 % for the OH PLIF images was in mean 2.2 pixels with a standard deviation at 1.1 pixels for the turbulent flames (F2-F4). For the quasi-laminar flame (F1) the mean difference was 1.7 pixels with a standard deviation of 0.7 pixels. A larger value of the OH threshold has a smaller difference since the isolines with larger threshold values move closer to the maximal OH gradient. The sensitivity of the flame position to the chosen threshold value was also evaluated. The difference in position between different threshold values was investigated whereas the difference between a threshold value of 5 % and 15 % is at most at 5 pixels for the turbulent flames and three pixels for the quasi-laminar flame. The same holds for the Toluene PLIF images when comparing the threshold values of 35 % and 45 %. Threshold values lower than the chosen ones were not preferred due to higher signal-to-noise ratio.

The ensemble averaged mean thicknesses of the overlapping region of CH_2O and toluene (marker of the preheat zone), the overlapping layer of OH and CH_2O (marker of the heat release layer), and the CH layer (marker of the inner layer) were determined as follows. First, the PLIF images were divided at the centerline (CL) into one left and one right part. A signal intensity profile for every pixel row, i.e. x/d, for each part was then investigated. A Gaussian function was fitted to the profiles and the full width at half maximum, FWHM, was used to define the thicknesses. For each flow speed a probability distribution function (PDF) over all the FWHMs, left and right, was investigated. The PDF has a beta-function shape profile, where the tail was considered to contain the FWHMs biased from 3D effects of the flame. Hence, a cut-off strategy was selected where the mean ($\bar{x}_{tot}$) and the standard deviation (σ_{tot}) for each PDF were calculated. The cut-off was then determined to discard all values > $\bar{x}_{tot}+ \sigma_{tot}$, which was ~15 % of the largest values. The thicknesses and its standard deviations represented in Figure 7 to 9 were then determined using the remaining samples after the cut-off. To validate the accuracy of the thicknesses, results with a cut-off at $\bar{x}_{tot}+ 2\sigma_{tot}$ were compared with those at $\bar{x}_{tot}+ \sigma_{tot}$. Since larger values

now was included the standard deviation and the mean thicknesses along the flame height increased. For flame F4 (which has the highest 3D bias error) the thicknesses increased with 8 % for the preheat zone, 11 % for the heat release layer and 15 % for the inner layer. Another source of 3D bias error worth of commenting is the laser sheet position over the jet nozzle. An offset from the center of the jet nozzle will affect the calculated thicknesses. A great care has been taken of the laser sheet position when setting up the experiment by iteration on a laminar flame for maximum flame waist.

3. Results and Discussion

3.1. *Turbulence field and global flame characteristics*

Figure 2 shows the mean axial velocity along the centerline of the burner under different center jet velocity conditions. In the measurements the flow of the pilot flame was kept constant, i.e., with a velocity of 0.4 m/s of the unburned stoichiometric methane/air mixture. The velocity and equivalence ratio of the center jet flow were varied to investigate the sensitivity of flow field to heat release from the flame. It is seen that the normalized velocity U/U_0 falls into one profile fairly well when the jet velocity is sufficiently high ($U_0 \geq 90$ m/s). The change of equivalence ratio has rather minor influence on the axial velocity field when the equivalence ratio is varied from 0.74 to 1, due to the minor change of flame temperature – the flame temperature varies by 16 % when the equivalence ratio is changed from 0.74 to 1. If the change of flame temperature is significantly larger, e.g. the mixture at the center jet is replaced by pure air, the velocity profile is significantly different from those presented in Figure 2. Furthermore, it is noted that the axial profile of the cases with $U_0 = 60$ m/s and 66 m/s are significantly different from those of higher jet velocities. The fact that the normalized axial velocity profiles of the high Reynolds number flows are nearly Reynolds number independent indicates that the flows with high jet velocity

($U_0 \geq 90$ m/s) is fully developed turbulent flows, whereas the flows with $U_0 = 60$ m/s and 66 m/s are not.

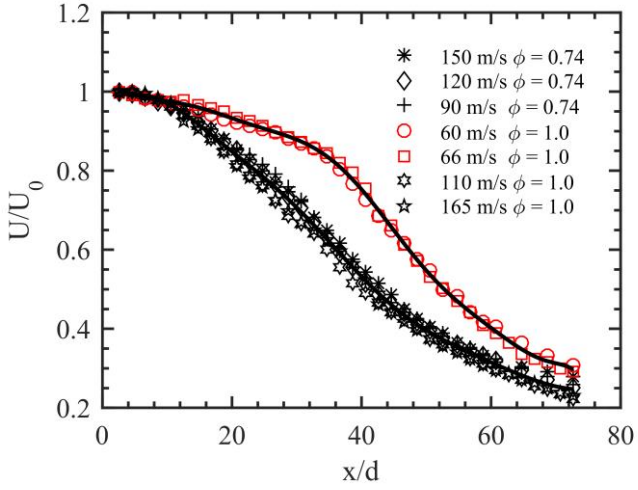

Figure 2. Mean axial velocity along the centerline of the burner.

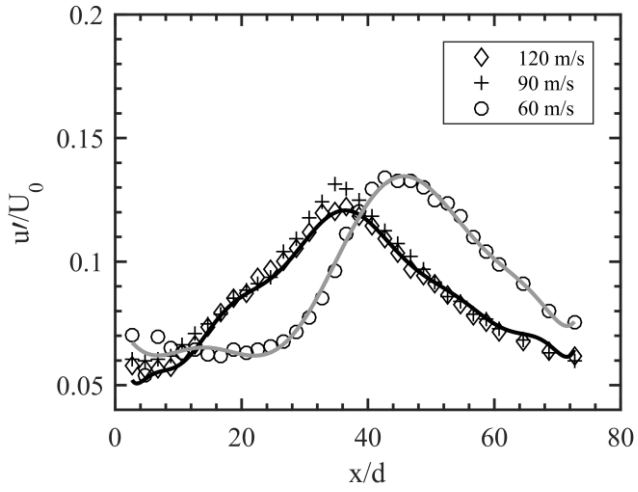

Figure 3. RMS of axial velocity fluctuations along the centerline of the burner.

Figure 3 shows the root-mean-square (rms) of the axial velocity fluctuations (u') along the centerline of the burner. The normalized rms axial velocity fluctuation (u'/U_0) is nearly Reynolds number independent when the jet velocity is high ($U_0 \geq 90$ m/s), which is consistent with the

behavior of the mean axial velocity field. u' is rather low near the burner exit ($x/d < 10$); further downstream, u' increases rapidly along the flame height, owing to the production of turbulence in the shear-layer of the jet flow. This process is continued until $x/d{\sim}35$ for the high jet velocity cases, where u'/U_0 reaches its peak, around 0.12; thereafter, u' decreases along the flame height due to dissipation of turbulence and relatively lower rate of turbulence production as a result of the lower mean velocity gradient downstream of the jet. For the lower Reynolds number flow cases ($U_0 = 60$ m/s and 66 m/s) u'/U_0 reaches its peak, around 0.14, at a further downstream position, $x/d{\sim}45$, which is a result of slower decay of the mean velocity field in these low Reynolds number flows, cf. Figure 2.

The mean axial velocity and its rms fluctuation along radial positions at different flame heights are measured. The mean axial velocity follows a nearly Gaussian distribution along the radial direction, from which one can calculate the width of the shear layer, namely the FWHM of the axial velocity profile. This length is used to represent the length scale of the large energy-containing eddies [37,38]. Figure 4 shows the trend of this large eddy length scale (ℓ_0) along the flame height for various flow speeds and equivalence ratios, including the cases of F2-F4 at two flame heights (x/D of 23 and 33). It appears that nearly all data falls into one profile, indicating that the width of the shear layers is rather Reynolds number independent.

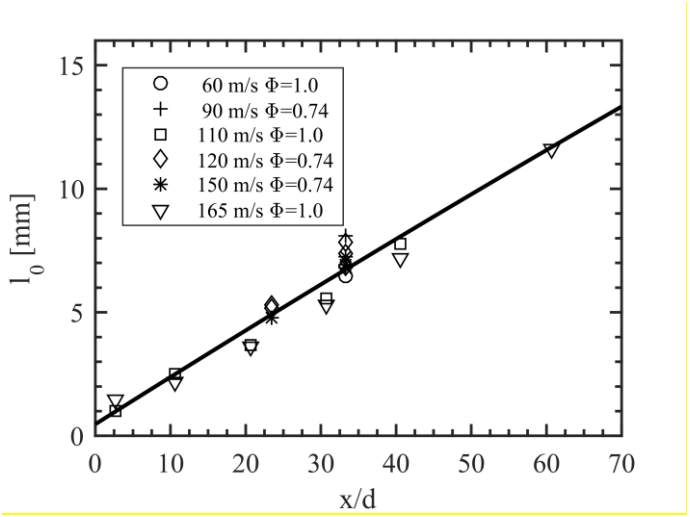

Figure 4. Integral length along the flame height.

Based on u' and ℓ_0 presented in Figs. 3 and 4 one can compute the characteristic non-dimensional parameters discussed earlier, e.g. the Karlovitz number. Figure 5 shows the Karlovitz number along the flame height. Near the burner exit the Karlovitz number is first decreasing along the flame height due to the increase of the large eddy length ℓ_0, and then it increases along the flame height due to the rapid increase of u', reaching a peak around the position where u' reaches its peak. Finally, the Karlovitz number decreases rapidly along the flame height due to the increase of ℓ_0 and the decrease of u'. For flame F2 the peak Karlovitz number is about 25; for flame F3 it is about 40, and for flame F4 the peak Karlovitz number is about 60. In the calculation of Karlovitz number the laminar flame speed and laminar flame thickness are based on a numerical calculation using the GRI 3.0 mechanisms [39], which gives that S_L=37.5 cm/s; δ_L=0.44 mm [40]. At the peak Karlovitz number position the Reynolds numbers based on the large energy containing eddies are 400, 424, and 570 for flames F2, F3 and F4, respectively. The corresponding turbulence intensities are $u'/S_L = 22$, 29, and 38 for flames F2, F3 and F4, respectively. A summary of these key parameters is given in Table 1. Flames F0 and F1 are laminar and quasi-laminar flames, respectively, in which the above-discussed non-dimensional parameters are not relevant. According

to the regime classification of Peters [3] flames F2, F3 and F4 are in the thin-reaction zone regime. Flame F0 and F1 can be used as a reference to represent the flame of flamelet case with Karlovitz number of 1.

It should be pointed out that ℓ_0 determined using the FWHM of the axial velocity profile is only a rough estimation of the integral length scale. More accurate methods exist, for example, based on the two-point velocity correlations [41] or based on the Taylor's frozen flow hypothesis with single-point velocity data [28,29]. However, these methods could not be applied here due to the limited temporal resolution in the present LDV measurements. The value of ℓ_0 reported in Fig. 4 is considered to be relevant only on the order of magnitude sense.

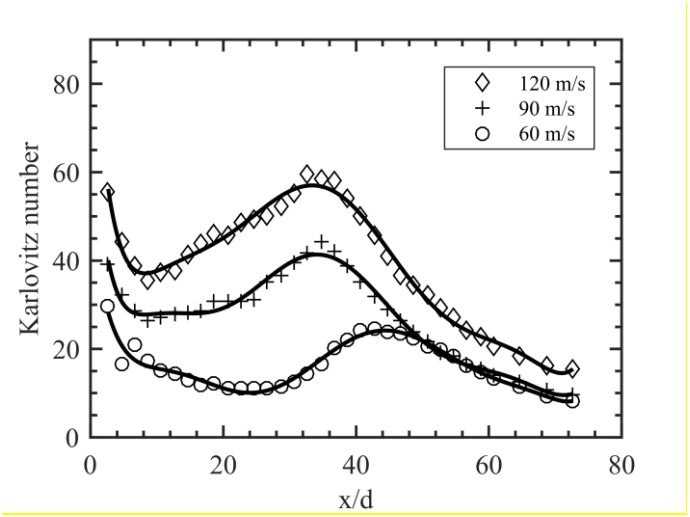

Figure 5. Karlovitz number along the flame height.

3.2. *Overall flame structures*

Figure 6 shows snap-shots of simultaneous PLIF imaging of four species, OH, CH, CH_2O and fuel tracer toluene ($C_6H_5CH_3$) above the burner at various jet velocities. Two PLIF signals are plotted in each of the images, i.e., OH/CH, CH/CH_2O, and CH_2O/$C_6H_5CH_3$. The laminar flame F1 shows rather thin CH layer throughout the entire flame. The fuel region is enclosed by a thin

layer of CH_2O, which is then enclosed by a thin layer of CH, and then outside the CH layer a thick OH layer can be found. The Reynolds number of flame F1 defined at the burner exit is 2900. Under this Reynolds number condition the flame is shown to be laminar; the low part of the flame is steady whereas at the upper part the flame (x>35 mm) is slightly unsteady likely due to the Rayleigh-Taylor instabilities [2]. With the jet velocity increased to 60 m/s the flame becomes highly unsteady. An increase in wrinkling of the CH layer at small scales is noticed; furthermore, formation of flame pockets enclosed by the CH layer, which are disconnected from the main flame, can be observed at the upper part of the flame of F2 (U_0 = 60 m/s). Within the pockets a mixture of toluene and CH_2O can be found. The pockets are surrounded by the thick OH region, indicating that the pockets are being oxidized. The formation of separated flame pockets appears to be more frequent with increasing U_0. The overlap regions of OH/CH, CH/CH_2O, and CH_2O/$C_6H_5CH_3$ are indicated using the white color in Figure 6. It is shown that rather significant overlap of CH_2O and $C_6H_5CH_3$ can be observed in the inner part of the flame for the three turbulent flames, whereas for the laminar flame F1 the overlap is not as significant. CH_2O could not be oxidized in the lower temperature preheat zone [25]; thus, the overlap of CH_2O and $C_6H_5CH_3$ can be used as a marker of the preheat zone. The overlap of OH/CH and CH/CH_2O is in rather thin zones for all flames studied, and for the turbulent flames it is significantly thinner than the overlap region of CH_2O and $C_6H_5CH_3$. The overlapping layer will be quantified in further detail below.

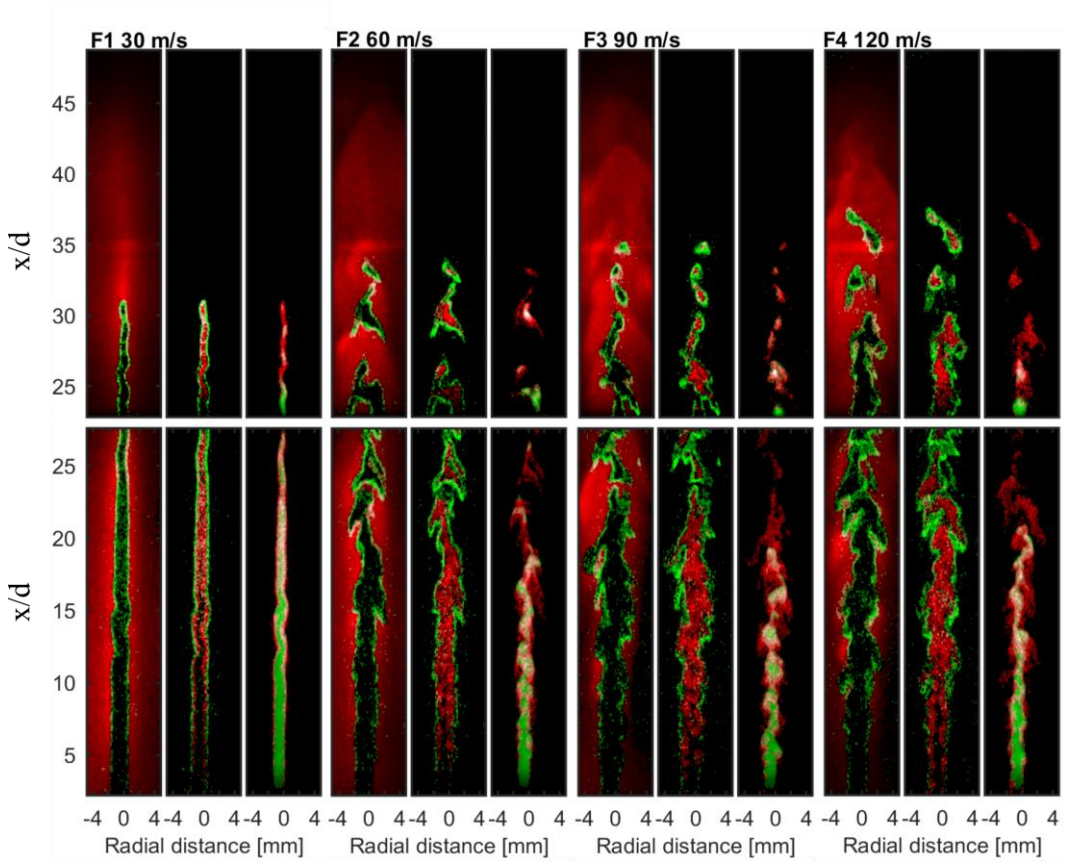

Figure 6. Snap-shots of the OH, CH, CH_2O and toluene PLIF images for the four flames. (F1) 30 m/s, (F2) 60 m/s, (F3) 90 m/s, and (F4) 120 m/s. Each set contains the following three images: left: OH (red) and CH (green), middle: CH_2O (red) and CH (green), right: CH_2O (red) and toluene (green) with the overlap between the two images highlighted with white.

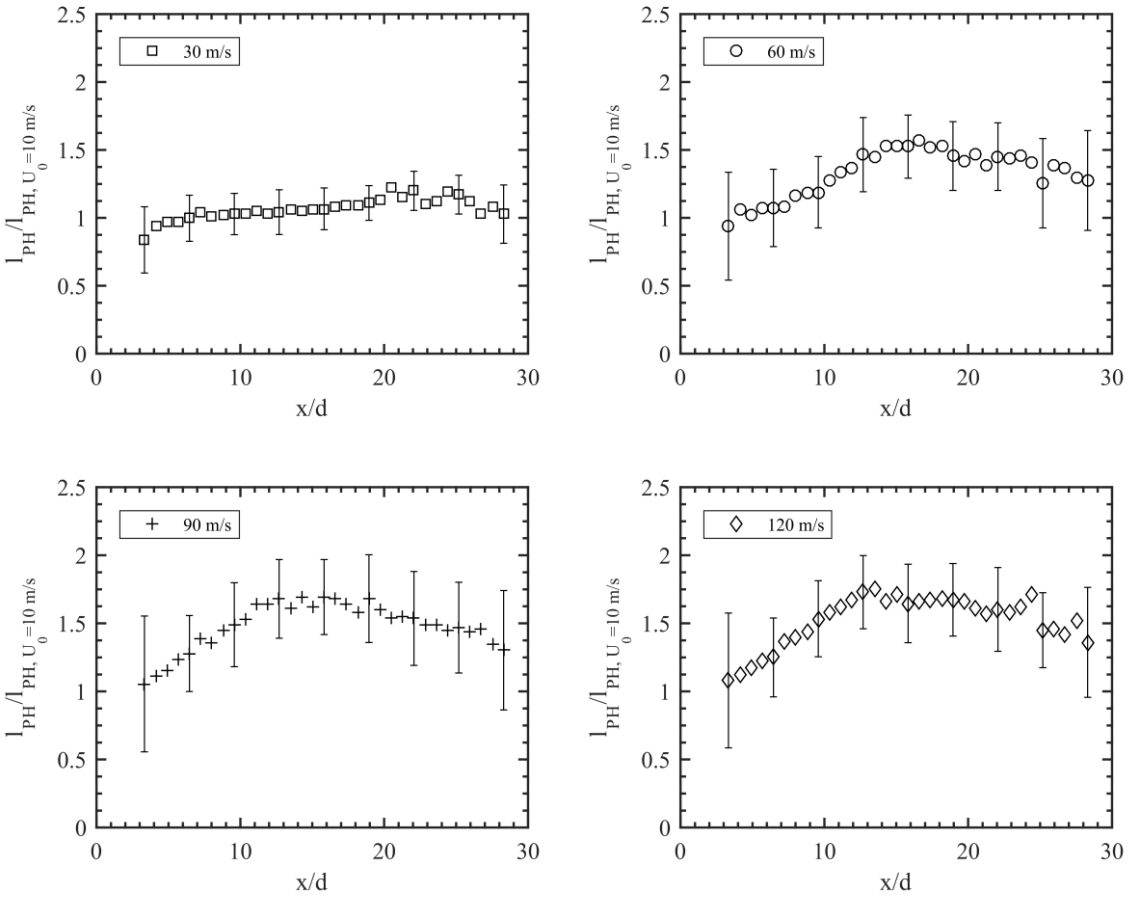

Figure 7. Ensemble averages of the thickness of the CH_2O/toluene overlapping layer along the flame height. Each flow speed is normalized by the thickness of the corresponding layer of the laminar flame case of U_0=10 m/s at x/d=7, which is about 0.42 mm.

Figure 7 shows the ensemble averaged mean thickness of the overlapping region of CH_2O and toluene (to indicate the preheat zone of the flame) along the flame height for the four flames. The thickness shown in Figure 7 has been normalized with the thickness of the corresponding overlapping layer in the laminar flame F0 at x/d=7, which is 0.42 mm. The laminar flame F1 shows a nearly constant thickness of the overlap region of toluene and CH_2O (~0.4 mm), which is consistent with the fact that in this flame the preheat zone is governed by molecular mixing and

thus the local flame structure remains similar along the flame height. The evaluated thickness scatters when approaching the flame tip, $x/d > 20$, due to the lower CH_2O and toluene intensity, which results in a lower signal-to-noise ratio. At the burner exit the flame is very thin owing to the jet flame configuration. The flow at the jet exit is at low turbulence intensity and the shear layer is thin; thus the preheat zone of all flames remains thin (about 0.4 mm – 0.5 mm). Along the flame height of the turbulent flames the thickness of the CH_2O and $C_6H_5CH_3$ overlapping region increases until $x/d{\sim}12$, which corresponds to the increase of the turbulent large eddy length scales and the turbulent kinetic energy (Figures 3 and 4). Comparing the three turbulent flame cases one notes that from flame F2 to flame F3 the thickness of the overlapping region increases with the jet Reynolds number (hence the intensity of turbulence). However, from flame F3 to flame F4 the thickness of the overlapping region does not change with the jet Reynolds number. The preheat zone of the flame appears to be self-similar at high Reynolds numbers, which is consistent with the self-similar behavior of the flow shown in Figures 2 and 3. For all turbulent flames the thickness of the overlapping region becomes nearly the same along the flame height when $x/d > 12$ due to the configuration of the jet flame. From Figure 6 it can be seen that the farthest downstream region of the toluene distribution is found at $x/d \sim 28$ ($x{\sim}42$ mm); the flame starts to shrink in the radial direction before reaching the tip (resulting in a conical flame shape). This confines the development of the preheat zone of all turbulent flames to a smaller region around the burner axis.

In a recent experimental study of pilot flame stabilized methane/air jet flames, Wabel et al. [29] showed a continuous development of the preheat zone thickness (defined using the CH_2O PLIF profile) with the jet Reynolds number. The studied jet has a relatively large diameter ($d{\sim}21.6$ mm), which allows for the development of thick preheat layers at high Reynolds numbers. For very large jet Reynolds numbers the data of Wabel showed also weak increase of the

preheat zone thickness with u'/S_L (viz. the jet Reynolds number), which is consistent with the present results.

The validity, consistency and accuracy in the quantification of the overlapping layers have to be considered. The major uncertainty in the length scale of the overlapping layers (l_{HR} and l_{PH}) is estimated to emerge from the finite spatial resolution in the binarized PLIF images and the detection limit of the measurement technique. Besides, and independent from this, there is also the temperature-dependent quenching rates impinging the results. Another factor to have in consideration, from both CH_2O and $C_6H_5CH_3$, is the inherent temperature dependence originating from the temperature dependence of the Boltzmann factor, which broadens the signal detected. Zhou et al [42] estimates the influence of the inherent temperature dependence for CH_2O. Its effect in relation to the spatial detection limit is negligible. To the authors knowledge no similar estimation of the inherent temperature dependence of the Boltzmann factor have been done for $C_6H_5CH_3$. However, toluene is known for its strong temperature dependence prompting a decrease in the quantum yield with increasing temperature due to enhanced quenching [43]. This will always be present; however, we believe that the general trends of the overlap are preserved, and its influence on the length scale to be considered as minor, the trends in the overlapping thickness are deliberated as consistent and valid.

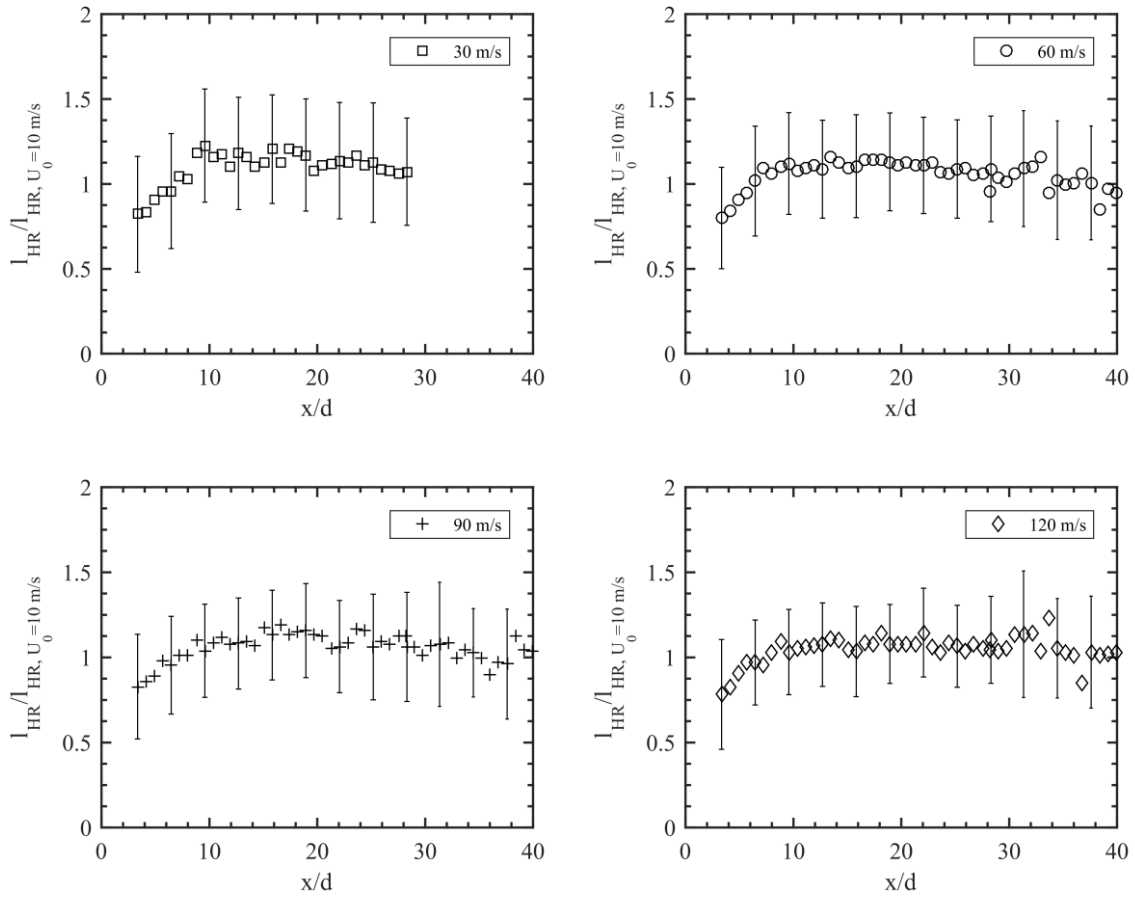

Figure 8. Ensemble averages of the thickness of the CH_2O/OH overlapping layer at different height above the burner. Each flow speed is normalized by the thickness of the corresponding layer of the laminar flame case of U_0=10 m/s at x/d=7, which is about 0.49 mm.

The ensemble averaged mean thickness of the overlapping layer of OH and CH_2O may be used to indicate the thickness of the heat release zone [22]. Figure 8 shows that the thickness of the overlapping layer of OH and CH_2O in all turbulent flames appears to be the same as that of the laminar flame. The thickness of overlapping region of OH and CH_2O increases from 0.4 mm to 0.55 mm in the near burner region ($x/d < 10$), due to the expansion of the jet flame. Thereafter, the thickness of the overlapping region of OH and CH_2O remains about 0.55 mm. This result is

consistent with the experimental results of Wabel et al. [29], where it was shown that the thickness of the overlapping region of OH and CH_2O remains nearly the same for the entire range of turbulent intensities studied, i.e., $u'/S_L \leq 243$.

Figure 9 shows the ensemble averaged mean thickness of the CH layer. The mean thickness of this layer for all turbulent flames is the same as that of the laminar one, and the thickness is also nearly a constant one (about 0.40 mm) along the flame height. As shown in Figure 6 the overlapping regions of CH/OH and CH/CH_2O are very thin, and the CH layer is in between the OH and the CH_2O layers. It is evident that the CH layer coincides rather well with the overlapping region of OH and CH_2O.

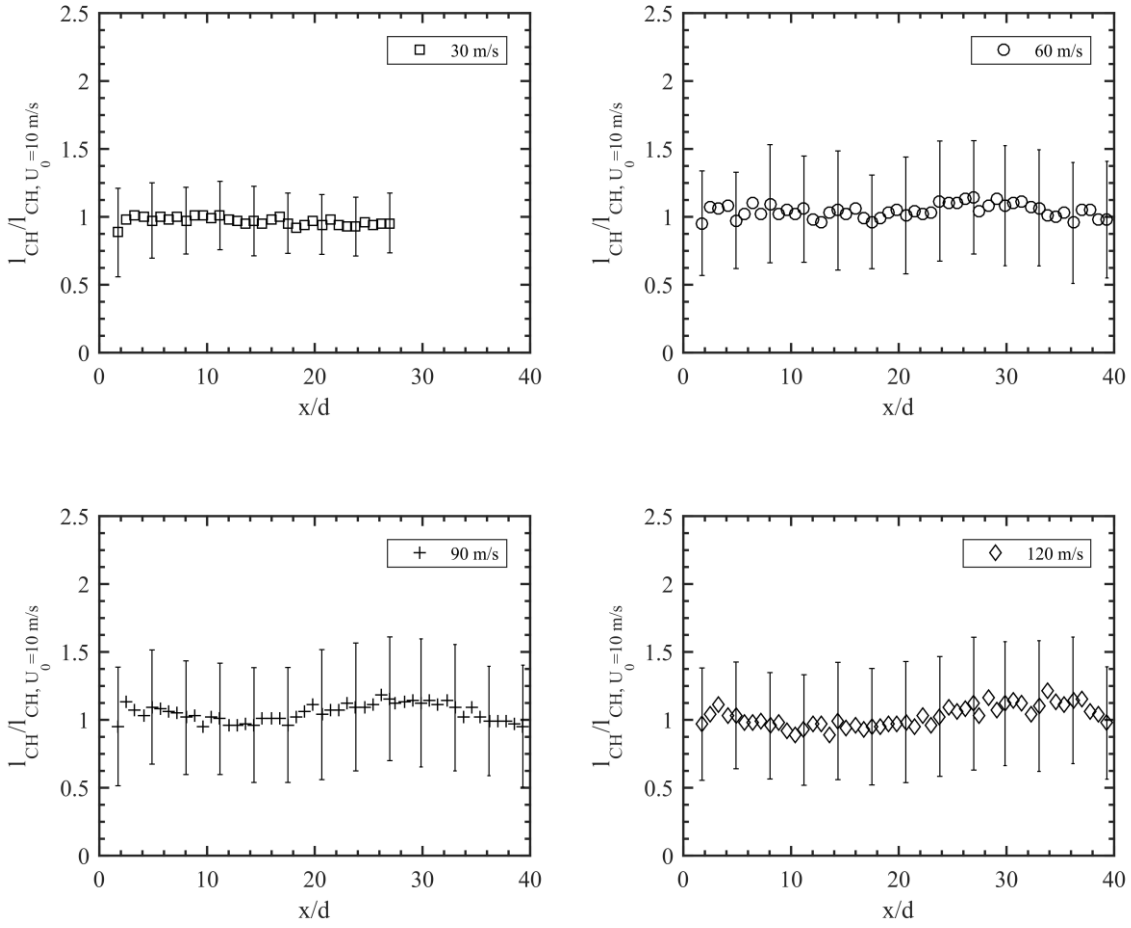

Figure 9. Ensemble averages of the thickness of the CH layer at different height above the burner. Each flow speed is normalized by the thickness of the corresponding layer of the laminar flame case of U_0=10 m/s at x/d=7, which is about 0.40 mm.

It should be pointed out that the present thicknesses are determined from 2D PLIF data, which is different from those of 3D flames. De Goey et al. [7] showed that the 3D thickness of a turbulent premixed methane/air flame was about 20 % smaller than the 2D thickness, while both the 2D and 3D thicknesses showed the same dependence on the turbulence intensity. The thickness of the reaction zone decreased with the turbulence intensity for lean premixed methane/air flames while it increased with the turbulence intensity for rich premixed methane/air flames. This is believed to be an effect of flame stretch. For stoichiometric flames the effect of flame stretch was shown to be rather minor; the thickness of the reaction zone of the strained flame remained similar to that of unstrained flames [7]. The present results are consistent with that of De Goey et al. [7] and the DNS results discussed in the Introduction section [12, 13]. Since the present flames are at stoichiometric conditions the effect of flame stretch on the thinning/thickening of the reaction layers is expected to be minor.

3.3. *Statistics of the flames*

The time averaged mean distributions of OH, CH, CH_2O and toluene PLIF signals are examined for various jet velocities. Since CH can be used as a reaction zone marker [4, 44] the mean CH layer depicts the time averaged mean flame brush. As seen in Figure 10, the laminar flame F1 (U_0 = 30 m/s) shows a typical conical flame structure where the CH layer remains thin throughout the entire flame. The turbulent flames F2, F3 and F4 show a broadening of the mean flame brush of

the mean reaction zone, owing to the highly unsteady motion of the reaction zone and the highly wrinkled reaction zone as shown in the instantaneous CH distribution in Figure 6. The thickness of the flame brush of the mean reaction zone (mean CH layer) increases along the flame height until about x~30 mm (x/d~20), thereafter the conical shaped flame becomes narrower in the radial direction due to the flame configuration. The CH_2O layer shows a tendency of broadening in the turbulent flames similar to that of the CH layers. Compared with the turbulent flames, the laminar flame F1 shows an OH field with a sharper edge, indicating a higher gradient. The mean toluene fields in the turbulent flames bear similarity and they are also broadened by turbulence.

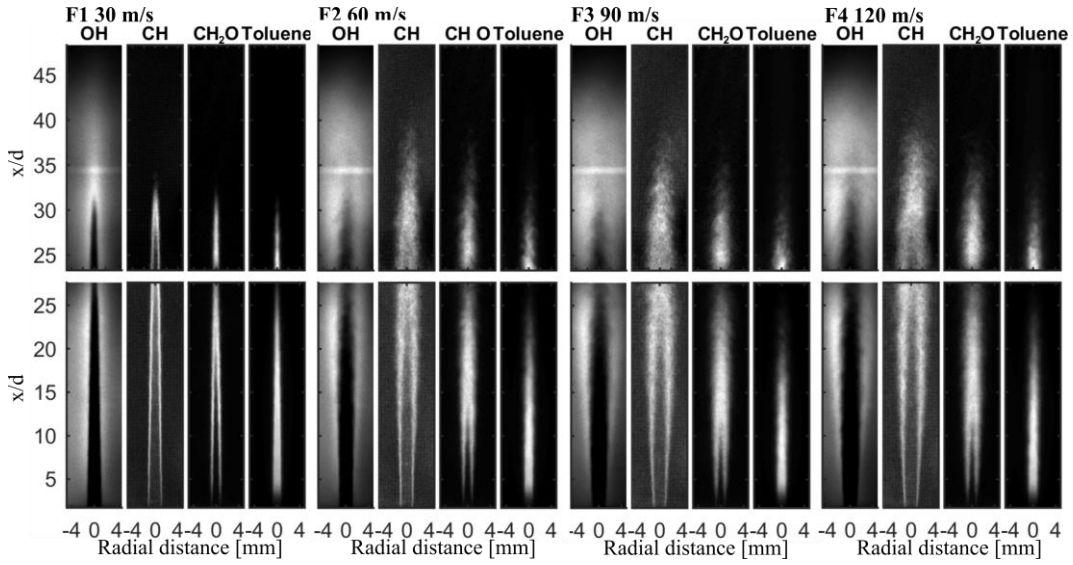

Figure 10. Time averaged OH, CH, CH_2O and toluene images. (F1) 30 m/s, (F2) 60 m/s, (F3) 90 m/s, and (F4) 120 m/s. Each set contains the following four mean fields, from left to right: OH, CH, CH_2O and toluene. The bright line artifact in the upper OH PLIF images is a reflection from the toluene/CH beam splitter.

The height of the flame may be defined as the length from the tip of the mean CH layer to the jet nozzle exit. It is seen that from flame F1 to flame F2 the height of the flame increases by about

10 mm, whereas further increase of the jet velocity does not result in further significant change of the flame height, cf. Figure 10. This indicates that the fuel consumption velocity increases with increasing turbulence intensity. Note that the tip of the reaction zone (indicated by the mean CH layer) is at $x\sim55$ mm or $x/d\sim36$, which coincides with the peak turbulence rms velocity in flames F3 and F4, cf. Figure 3. Thereafter, turbulence starts to decay rapidly. Comparing with the turbulence field of isothermal turbulent jet flows [45] it appears that the heat release has delayed the decay of turbulence to positions further downstream. The radial distribution of the axial velocity indicates that heat release in the reaction zone contributes to the production of turbulence by increasing the radial gradient of axial velocity in the shear layer.

Figure 11 shows the mean positions of OH layer, i.e. the $<c_{OH}>=0.5$, which indicates the oxidation layer of CO and H_2, and the toluene layer, i.e. the $<c_F>=0.5$, which indicates the fuel-consumption layer, where $<c_{OH}>$ and $<c_F>$ are the mean reaction progress variables based on the OH PLIF and toluene PLIF fields explained in section 2.4 *Data post-processing*. Both the OH front and the toluene front show noise fluctuations. This is due to the use of limited number of samples (100 samples) in the ensemble average of the binary OH and toluene fields. These are random noises that will disappear when the number of samples increases. To remove the noises, we have applied a 4^{th}-order polynomial fitting function to represent the mean fronts. It is expected that the polynomial fitted profiles are closer to the converged mean OH and toluene front.

The region in-between the two layers may be used to represent the width of the entire mean reaction zone. For the laminar flame F1 the two layers are close to each other in the main part of the flame, except the region around the flame tip where the toluene layer ends at $x/d\sim26$, whereas the OH layer ends at $x/d\sim30$. The broadening of the reaction zone in the flame tip is likely owing to several effects. First, the curvature effect of the conical flame where the reaction zones on the cone surface merges at the flame tip. Second, one can notice from Figure 6 that at the flame tip unburned fuel pockets are occasionally formed and separated from that of the main flame, which

will also give rise to a broader mean reaction zone. The OH layer and the toluene layer in the turbulent flames differ more significantly than that in the laminar flame. The OH layer expands more in the radial direction than that in the laminar flame whereas the toluene layer is less expanding in the radial direction. Flame dilatation effect gives rise to radial expansion of the OH layer more than that to the toluene layer since the heat release is mainly at the OH layer.

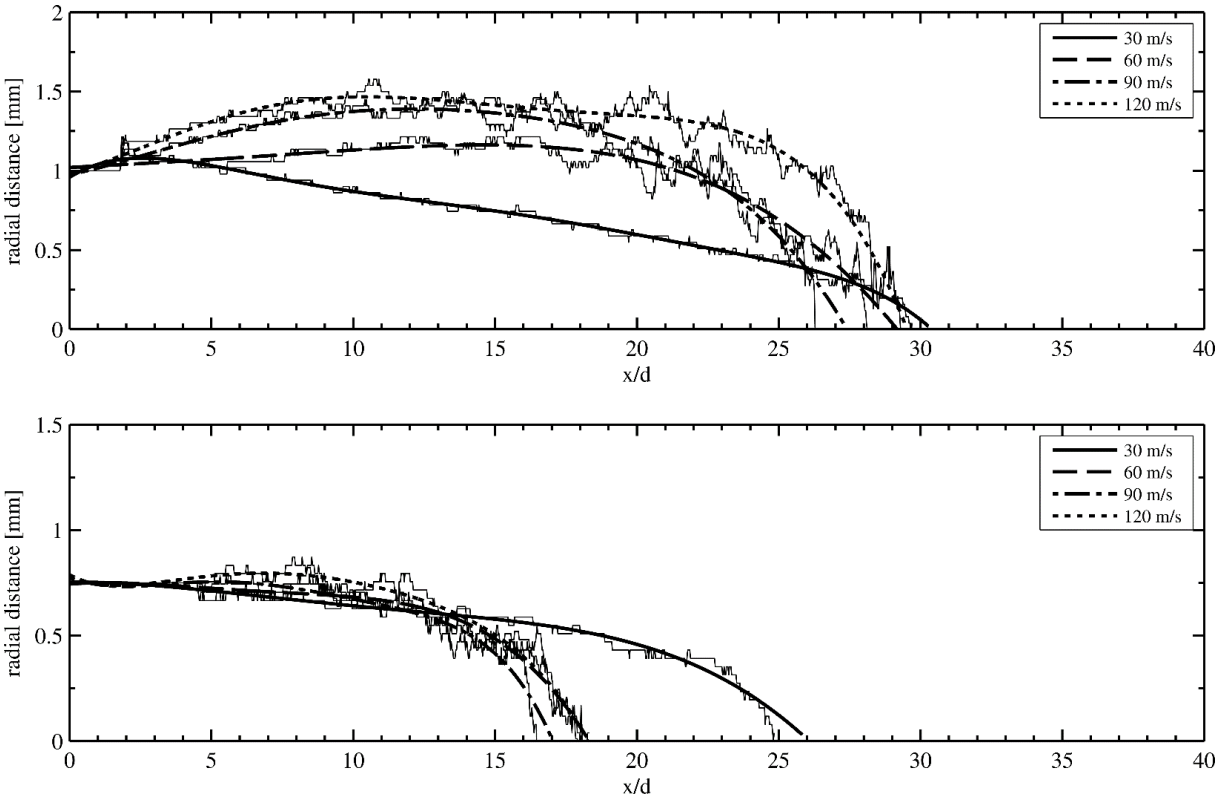

Figure 11. Mean flame position defined using (a) OH layer, (b) toluene layer. The thin lines are computed from the PLIF data; the thicker lines are 4th-order polynomial curve fittings of the data.

The toluene layers of the turbulent flames coincide with each other rather well, which is consistent with the Damköhler wrinkled flamelet theory. In the flamelet regime, the ratio of wrinkled flame surface area (A) to that of the mean flame surface area ($\bar{A}$) is proportional to the velocity of the large energy-containing eddies, $\sigma \sim A/\bar{A} \sim u'/S_L$. From Figure 3 it appears that $u' \sim cU_0$, where $c = u'/U_0$ is approximately independent of U_0, in particular for the high Reynolds number

flames. From mass conservation law, the mass flow rate of fuel supplied from the burner is equal to the fuel consumption rate at the flamelet, i.e., $\dot{m}_f \sim A S_L$. It follows that, $\bar{A} \sim A/\sigma \sim \dot{m}_f/(S_L \sigma) \sim U_0/(cU_0) \sim 1/c$, which is approximately independent of U_0. The results shown in Figure 11 are consistent with the above scaling, which provides an experimental support to the Damköhler wrinkled flamelet theory for the fuel-consumption layer, despite that the present turbulent flames have rather high Karlovitz numbers and they are in the thin-reaction zone regime.

The area of the mean OH layer in the turbulent flames differs between each other more noticeably than that of the toluene layer. From flame F2 to flame F3 the area increases by 50 %, and from F3 to F4 the area increases by another 30 %. The increase of the area of the mean OH layer with the jet velocity indicates that the oxidation of the intermediate fuels (e.g., CO and H_2) requires larger mean area to finish, which is not consistent with the Damköhler wrinkled flamelet theory discussed above.

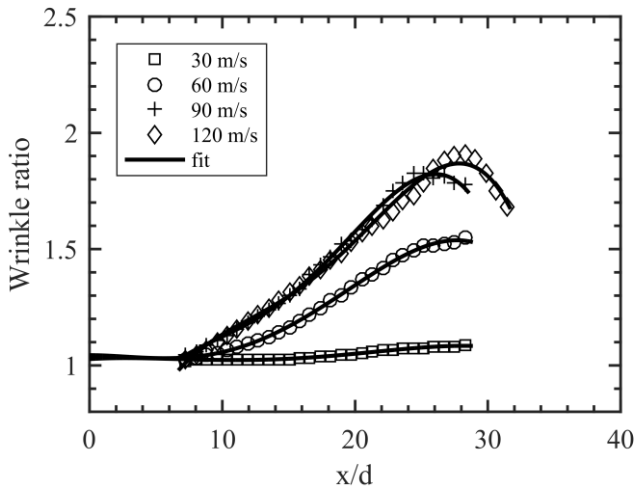

Figure 12. Flame surface wrinkle ratio at different height above burner.

It is likely that the wrinkled area of the OH layer does not increase with increasing jet velocity (U_0) and thus with increasing turbulent kinetic energy ($\sim u'^2$), so that the layer has to expand

either radially or along axial direction. To examine this, the flame surface wrinkle ratio $\sigma(x)$, based on the layer with the maximal gradient of OH (using Eq. 5), is computed. As discussed in section 2.4 the use of OH maximal gradient and a threshold value of 5 % of maximal OH intensity to define the instantaneous OH front gives a difference about 2.2 pixels, which is significantly smaller than the smallest wrinkle scales (about 10 pixels). No noticeable difference in the profile of $\sigma(x)$ could be observed when using the two different methods.

Figure 12 shows that $\sigma(x)$ in the laminar flame F1 is nearly constant and equals to 1, which is consistent with the fact that flame F1 is not wrinkled (cf. Figure 6). The turbulent flames F2 – F4 show an increase of $\sigma(x)$ along the flame height, which is consistent with the increase of turbulent rms velocity (u') along the flame height. At further downstream $\sigma(x)$ decreases with x, due to the formation of flame holes, which gives rise to a lower flame surface area when part of the holes locates within the sampling window. Compared with flames F3 and F4, flame F2 has a lower flame surface wrinkle ratio due to the lower turbulence intensity. From Figures 2 and 3 it is noted that flame F2 is not a fully developed turbulent flame, which is contributing to the low degree of flame wrinkling as indicated in Figure 12.

It is interesting to note that the flame surface wrinkle ratio becomes Reynolds number independent when the jet velocity is high, e.g. flames F3 and F4. In the lower part of the flame $\sigma(x)$ of flame F3 is nearly identical to that of F4; it does not increase with increasing u'. Since the length scale of the large energy-containing eddies for all three turbulent flames are approximately the same, the increase of u' would imply a decrease of the length scale of Kolmogorov eddies. In the Damköhler flamelet model the decrease of the length scale of Kolmogorov eddies would give rise to the formation of the smaller wrinkle scales by the Kolmogorov eddies. The fact that the wrinkling scales stop decreasing indicates that when the turbulence eddies are small enough they are not effective in wrinkling the flame. This result is consistent with the DNS results of Doan et

al. [46], in which the authors applied a multi-scale analysis of five DNS datasets for premixed flames in the laminar flamelet and the thin reaction zone regimes. Doan et al. showed that eddies smaller than $2\delta_L$ contribute less than 10% of the total tangential strain rate, indicating that small scale structures have a reduced influence on the flame.

The minimal wrinkle scale measured in the present experiments may be compared with the Gibson scale in the flamelet regime [3], below which further wrinkling of the flame is not effective. The Gibson length is larger than the Kolmogorov length. Based on heuristic argument that the smallest winkle scale is when eddy velocity of that scale is on the same order of the laminar burning velocity it was shown that the Gibson length decreases with the increase of u' [47],

$$\ell_G \sim {S_L}^3/\varepsilon \sim \ell_0(S_L/u')^3 \sim \delta_L Ka^{-2} \tag{9}$$

where $\varepsilon \sim u'/\ell_0$ is the dissipation rate of turbulent kinetic energy and use of Eq. (1) is made. Gulder and Smallwood [48] reviewed various empirical expressions of the Gibson length in the literature and they found that a large body of experiments fit to the expression of $\ell_G \sim \delta_L Ka^{\beta}$, where $\beta \simeq -1/2$, for Ka numbers up to 5.

The present experimental results show that the smallest wrinkle scale is consistent with the literature for small Ka flames (from F2 to F3) while at higher Ka the small wrinkle scale is independent of Ka. Investigation of the spectrum of the wrinkle scale shows that when Ka is large enough (flames F3 and F4) the smallest wrinkle scales are on the order of the thickness of the heat release layer (ca. 0.4 mm). Further decrease of the wrinkle scales is therefore not possible. This cutoff wrinkle scale is much larger than the Kolmogorov length in these flames (cf. Table 1) and it is also well above the spatial resolution of the current PLIF setup. The present results are consistent with the DNS results of Poludnenko and Oran [10]. Their DNS data suggest that the estimation from Eq. (9) in the thin-reaction regime is four orders of magnitude smaller than δ_L. However, smaller scales than δ_L could not survive the rapid temperature increase across the flame.

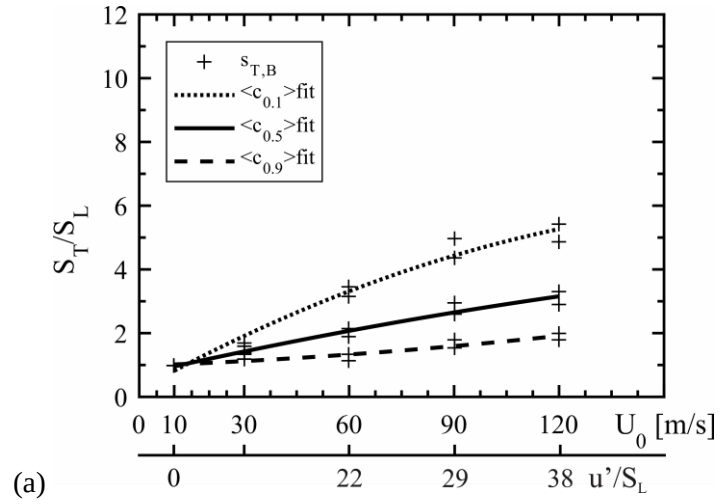

(a)

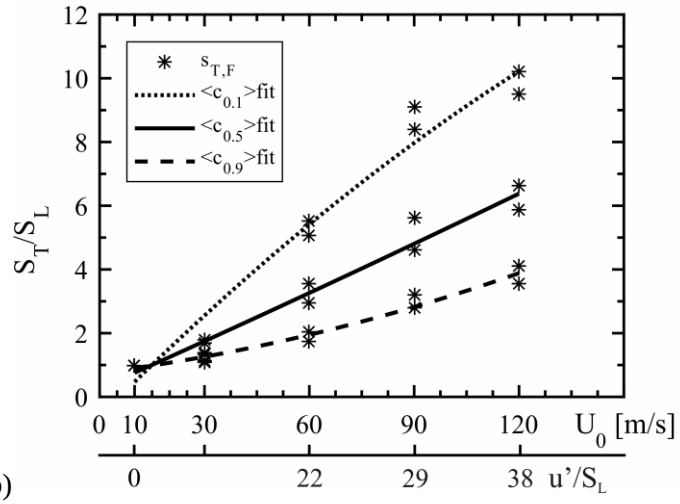

(b)

Figure 13. Turbulent consumption speed defined using the OH layer (a) and the toluene layer (b). For each layer two datasets are shown in the figure, since calculation of the mean area $\bar{A}$ using Eq. (7) requires only one. At U_0=30 m/s the flame is unsteady and quasi-laminar; thus, $u'/S_L \sim 0$. Note that u' is not linearly scaling with U_0, cf. Fig.3 and Table 1.

An important parameter characterizing the turbulent flames is the turbulent burning velocity. Three different turbulent burning velocities can be defined for a flame, the local turbulent displacement speed of a layer in the flame, the local turbulent fuel consumption velocity, and the global turbulent fuel consumption velocity [4]. The first two burning velocities require spatially

resolved simultaneous PIV and PLIF data. The global turbulent fuel consumption velocity ($S_{C,T}$) can be estimated based on the mean flame surface area, i.e., Eq.(8), rewritten in terms of the volume flow rate of the fuel/air mixture, $\dot{m}_f$,

$$S_{C,T} = \dot{m}_f / A, \tag{9}$$

where A is determined using Eq.(7). Some authors use the mean flame surface area defined in the position of the OH <c> iso-contour [4]. Alternatively, one may use the flame surface based on the toluene (fuel-consumption) layer to compute $S_{C,T}$. The value of $S_{C,T}$ is sensitive to iso-contour of <c>. Kobayashi et al. [49] compared the values of surface area of <c>=0.05, 0.1, and 0.5. They showed that the surface area of <c>=0.5 is significantly larger than those of <c>=0.1 and 0.05. The flame surface area defined at <c>=0.1 and 0.05 are very similar.

Figure 13 shows $S_{C,T}$ computed using the <c>=0.1, 0.5 and 0.9 surfaces of OH and toluene. $S_{C,T}$ in the figure is normalized with the corresponding global fuel consumption velocity of the laminar flame F0. Since the flame is not perfectly axisymmetric the calculation of the mean area $\bar{A}$ using Eq. (7) would give slightly different results if different sides of the mean layer with respect to the jet axis were used. To show the data scatter due to the slight asymmetry of the jet, two datasets are shown in the figure, with each dataset computed using different side of the mean layer profile. From Fig. 13 it is shown that the value of $S_{C,T}$ scatters within $\pm 0.42 S_L$, which indicates the uncertainty of $S_{C,T}/S_L$ due to the asymmetry of the jet is about 5% for flame F4 determined using $<c_f>$=0.1. Furthermore, in calculation of the mean flame front area used in Eq. (9) the mean flame fronts with polynomial de-noised profile is used since these profiles smoothened away random noises in the mean flame front caused by the lack of experimental samples in the ensemble average of the mean flame front. With random noise included in the mean flame front the area is about 10 % higher than the de-noised ones. The overall trend of the turbulent burning velocity with respect to change of the turbulence intensity is however the same with or without the de-

noise operation. The uncertainty of $S_{C,T}$ due to the uncertainty of the volume flow rate $\dot{m}_f$ is rather low, about 1%.

From Fig. 13 it is clear that the value of $S_{C,T}$ is sensitive to the values of <c> selected. If the iso-surfaces of <c>=0.1 is used, the values of $S_{C,T}/S_L$ varies from 1 to 5.4 (from flame F0 to flame F4 based on the OH field) and 10.2 (based on toluene). The two turbulent burning velocities differ by a factor of 2. The turbulent burning velocity defined on the toluene layer is nearly a linear function of the turbulence intensity u'/S_L. This is owing to the nearly Reynolds number independent mean flame surface area at the toluene (fuel-consumption) layer, which implies that the fuel-consumption layer behaves like a wrinkled laminar flamelet. The global turbulent fuel consumption speed based on the OH layer increases with u'/S_L, initially linearly, and then slower than the initial increase rate at high turbulence intensities, e.g. from flame F3 to F4. The slower increase of the fuel consumption speed is owing to the fact that the mean position of the OH layer expands continuously in the radial and axial direction, cf. Figure 11. This phenomenon is known as fall-off from the linear dependence of u'/S_L, which has been reported in the literature, e.g., by Peters [3]. The fall-off of S_T from linear dependence of u'/S_L is an indication that the oxidation layer is of a non-flamelet type flame structure.

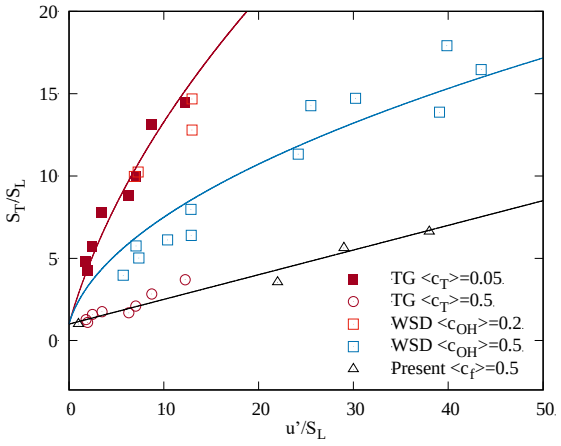

Figure 13. Turbulent fuel consumption velocity as a function of u'/S_L, with results from Tamadonfar and Gülder (TG) [41], Wabel et al. (WSD) [28], and the present experiments defined on the iso-surface of toluene PLIF. The solid lines are trend lines of the experimental data.

It is noted that the global turbulent fuel consumption velocities from different experimental rigs differ greatly [4, 50-52]. In Fig. 14 the present results are compared with the recent results of Wabel et al. [28] and the data from Tamadonfar and Gülder [41]. The data from Wabel et al. was defined on $<c_{OH}>$=0.2 and 0.5. The data from Tamadonfar and Gülder [41] was defined on $<c_T>$=0.05 and 0.5, where c_T is the reaction progress variable defined using the temperature field, which is equivalent to the present c_f defined using the toluene PLIF. It is seen that $S_{C,T}$ of Tamadonfar and Gulder [41] defined at $<c_T>$=0.5 is about 3-4 times smaller than the corresponding one at $<c_T>$=0.05, whereas $S_{C,T}$ of Wabel et al. defined at $<c_{OH}>$=0.5 is about 2 times smaller than those at $<c_T>$=0.2. Our data defined at $<c_f>$=0.5 are in reasonable agreement with that of Tamadonfar and Gulder [41] defined at $<c_T>$=0.5.

The difference between the present data and data from Wabel et al. is likely due to the following differences in the experimental rig. First, in the present experiments the burner diameter (d=1.5 mm) is much smaller than that of Wabel et al. (d=21.6 mm). With a larger burner diameter the flame can allow for more wrinkle scales to develop, which results in higher $S_{C,T}$. Second, in the burner of Wabel et al. a slotted plate turbulence generator is employed upstream of the converging nozzle, which can give a very high turbulent intensity ($u'/U_0 \sim 0.47$) at the burner exit. This allows for intensive flame/turbulence interaction already in the proximity of the burner exit. As a result, the flame height is much shorter ($1d - 4d$), thereby a much higher $S_{C,T}$. Our burner does not employ a turbulence generator inside the burner. Turbulence is generated in the shear layer of the flow with the highest turbulent intensity $u'/U_0 \sim 0.14$ achieved at $x/d \sim 30 - 40$. In

the proximity of the burner exit the turbulent intensity is low and the flame surface is not highly wrinkled, cf. Fig.6, and the DNS results of Wang et al. [53] for the present burner at $U_0 = 110$ m/s (cf. Fig.2 of Ref. [53]). As a result of the low turbulence intensity in the proximity of the burner the flame height of the present burner is much longer than those of Wabel et al. [28], which results in a lower $S_{C,T}$, according to Eqs. (7-9).

4. Conclusions

The structures of turbulent methane/air premixed jet flames in the flamelet and thin-reaction regimes are studied using simultaneous Planar Laser-Induced Fluorescence (PLIF) imaging of CH, OH, CH_2O and toluene, and Laser Doppler Anemometry (LDA). The jet Reynolds number ranges from 960 to 11500, and the Karlovitz number ranges from 1 to 60. The goals are to quantify the thickness and wrinkling of different sub-layers in the flames under different levels of turbulence, and to reconcile several model hypotheses. The main findings are summarized as follows.

- The preheat zone of the flames characterized using the overlapping layer of CH_2O and toluene is progressively thickened by turbulence along the flame height due to the increased thickness of the mixing layer and the increased turbulence intensity. The thickness of the preheat zone is sensitive to the intensity of turbulence; for low and moderate Reynolds number flames the thickness of the preheat zone increases with Reynolds number, while at high Reynolds numbers the thickness of the preheat zone becomes Reynolds number independent. This is likely due to the present flame configuration; at high Reynolds numbers the present jet turbulent flow becomes self-similar and the thickness of the mixing layer (thus the integral length scale of turbulence) is Reynolds number independent.
- The overlapping layer of CH_2O and OH, which is often used to characterize the heat release layer, remains thin in all flames. The CH layer, which may be used to denote the

fuel-consumption layer, also remains thin in all flames studied. The mean position of the fuel consumption layer (defined using the reaction progress variable based on the toluene PLIF field) is rather insensitive to the variations of Reynolds number, while the mean position of the oxidization layer of CO and H_2 (defined using the reaction progress variable based on the OH PLIF field) is rather sensitive to the variations of Reynolds number. The distance between the mean position of the fuel-consumption layer and the mean position of the oxidization layer, which may be used to define the mean thickness of the reaction layer, increases with the Reynolds number. This finding provides the experimental support of Peters' thin-reaction zone theory, which is based on the assumption that in the thin-reaction zone regime the thickness of the fuel-consumption zone remains thin while the oxidization zone is broadened by turbulence.

- For low and moderately high Karlovitz numbers (< 40) the flame surface wrinkle ratio defined at the OH layer is shown to increase with flame height (due to the increase in both the turbulence intensity and length scale), and also with the jet Reynolds number (and Karlovitz number). This indicates that the smallest wrinkle scales decrease with Karlovitz number. This is consistent with the literature empirical expressions of the Gibson scale, which is the smallest wrinkle scale of the flame.
- For high Karlovitz number flames ($Ka>40$) the flame surface wrinkle ratio becomes Reynolds number (and Karlovitz number) independent. Since the Kolmogorov scale decreases with the jet Reynolds number it appears that the small eddies at high Reynolds numbers do not effectively wrinkle the flame. It is shown that when the theoretical Gibson length developed for the laminar flamelet regime is smaller than the thickness of the heat release zone it becomes irrelevant in the wrinkling of the flames.

Acknowledgements

The authors acknowledge financial support from the Swedish Energy Agency through CECOST (Centre for Combustion Science and Technology) and the Swedish-Chinese collaboration project (Project No. 33305-1), VR (Swedish Research Council), and the European Research Council Advanced Grant TUCLA.

References

[1] R. Borghi, Turbulent combustion modelling, Prog. Energy Combust. Sci. 14 (1988) 245-292.
[2] F. Williams, Combustion theory, Benjamin Cummings, Menlo Park, CA, 1985.
[3] N. Peters, Turbulent combustion, Cambridge University Press, Cambridge, 2000.
[4] J.F. Driscoll, Turbulent premixed combustion: Flamelet structure and its effect on turbulent burning velocities, Prog. Energy Combust. Sci. 34 (2008) 91-134.
[5] I.G. Shepherd, R.K. Cheng, T. Plessing, C. Kortschik, N. Peters, Premixed flame front structure in intense turbulence, Proc. Comb. Inst. 29 (2002) 1833-1840.
[6] P. Tamadonfar, Ö.L. Gülder, Experimental investigation of the inner structure of premixed turbulent methane/air flames in the thin reaction zones regime, Combust. Flame 162 (2015) 115-128.
[7] L.P.H. de Goey, T. Plessing, R.T.E. Hermanns, N. Peters, Analysis of the flame thickness of turbulent flamelets in the thin reaction zones regime, Proc. Comb. Inst. 30 (2005) 859-866.
[8] K. Seshadri, N. Peters, The inner structure of methane-air flames, Combust. Flame 81 (1990) 96-118.
[9] T. Poinsot, D. Veynante, S. Candel, Quenching processes and premixed turbulent combustion diagrams, J. Fluid Mech. 228 (1991) 561-606.
[10] A.Y. Poludnenko, E.S. Oran, The interaction of high-speed turbulence with flames: Global properties and internal flame structure, Combust. Flame 157 (2010) 995-1011.
[11] Y.-S. Shim, N. Fukushima, M. Shimura, Y. Nada, M. Tanahashi, T. Miyauchi, Radical fingering in turbulent premixed flame classified into thin reaction zones, Proc. Comb. Inst. 34 (2013) 1383-1391.
[12] R. Sankaran, E.R. Hawkes, C.S. Yoo, J.H. Chen, Response of flame thickness and propagation speed under intense turbulence in spatially developing lean premixed methane–air jet flames, Combust. Flame 162 (2015) 3294-3306.
[13] A.J. Aspden, M.S. Day, J.B. Bell, Three-dimensional direct numerical simulation of turbulent lean premixed methane combustion with detailed kinetics, Combust. Flame 166 (2016) 266-283.
[14] Y.-C. Chen, R.W. Bilger, Simultaneous 2-D Imaging Measurements of Reaction Progress Variable and OH Radical Concentration in Turbulent Premixed Flames: Experimental Methods and Flame Brush Structure, Combust. Sci. Technol. 167 (2001) 131-167.
[15] Y.-C. Chen, R.W. Bilger, Simultaneous 2-D Imaging Measurements of Reaction Progress Variable and OH Radical Concentration in Turbulent Premixed Flames: Instantaneous Flame-Front Structure, Combust. Sci. Technol. 167 (2001) 187-222.

[16] Y.-C. Chen, R.W. Bilger, Experimental investigation of three-dimensional flame-front structure in premixed turbulent combustion—I: hydrocarbon/air bunsen flames, Combust. Flame 131 (2002) 400-435.
[17] Y.-C. Chen, R.W. Bilger, Experimental investigation of three-dimensional flame-front structure in premixed turbulent combustion: II. Lean hydrogen/air Bunsen flames, Combust. Flame 138 (2004) 155-174.
[18] C. Kortschik, T. Plessing, N. Peters, Laser optical investigation of turbulent transport of temperature ahead of the preheat zone in a premixed flame, Combust. Flame 136 (2004) 43-50.
[19] M.J. Dunn, A.R. Masri, R.W. Bilger, A new piloted premixed jet burner to study strong finite-rate chemistry effects, Combust. Flame 151 (2007) 46-60.
[20] M.J. Dunn, A.R. Masri, R.W. Bilger, R.S. Barlow, Finite Rate Chemistry Effects in Highly Sheared Turbulent Premixed Flames, Flow Turbul. Combust. 85 (2010) 621-648.
[21] F.T.C. Yuen, Ö.L. Gülder, Dynamics of Lean-Premixed Turbulent Combustion at High Turbulence Intensities, Combust. Sci. Technol. 182 (2010) 544-558.
[22] H.N. Najm, P.H. Paul, C.J. Mueller, P.S. Wyckoff, On the Adequacy of Certain Experimental Observables as Measurements of Flame Burning Rate, Combust. Flame 113 (1998) 312-332.
[23] Z.M. Nikolaou, N. Swaminathan, Heat release rate markers for premixed combustion, Combust. Flame 161 (2014) 3073-3084.
[24] J. Sjöholm, J. Rosell, B. Li, M. Richter, Z. Li, X.-S. Bai, M. Aldén, Simultaneous visualization of OH, CH, CH2O and toluene PLIF in a methane jet flame with varying degrees of turbulence, Proc. Comb. Inst. 34 (2013) 1475-1482.
[25] Z.S. Li, B. Li, Z.W. Sun, X.S. Bai, M. Aldén, Turbulence and combustion interaction: High resolution local flame front structure visualization using simultaneous single-shot PLIF imaging of CH, OH, and CH2O in a piloted premixed jet flame, Combust. Flame 157 (2010) 1087-1096.
[26] B. Zhou, C. Brackmann, Z. Li, M. Aldén, X.-S. Bai, Simultaneous multi-species and temperature visualization of premixed flames in the distributed reaction zone regime, Proc. Comb. Inst. 35 (2015) 1409-1416.
[27] B. Zhou, C. Brackmann, Z. Li, M. Aldén, X.-S. Bai, Thin reaction zone and distributed reaction zone regimes in turbulent premixed methane/air flames: Scalar distributions and correlations, Combustion and Flame 175 (2017) 220-236.
[28] T. M. Wabel, A. W. Skiba, J. F. Driscoll, Turbulent burning velocity measurements: extended to extreme level of turbulences, Proc. Comb. Inst. 36 (2017) in press.
[29] T. M. Wabel, A. W. Skiba, J. E. Temme, J. F. Driscoll, Measurements to determine the regimes of premixed flames in extreme turbulence, Proc. Comb. Inst. 36 (2017) in press.
[30] J. Hult, M. Richter, J. Nygren, M. Aldén, A. Hultqvist, M. Christensen, B. Johansson, Application of a high-repetition-rate laser diagnostic system for single-cycle-resolved imaging in internal combustion engines, Appl. Opt. 41 (2002) 5002-5014.
[31] C.F. Kaminski, J. Hult, M. Richter, J. Nygren, A. Franke, M. Aldén, S. Lindenmaier, A. Dreizler, U. Maas, R.B. Williams, Development of high speed spectroscopic imaging techniques for the time resolved study of spark ignition phenomena, SAE Technical Paper 2000-01-2833 (2000).
[32] J. Sjöholm, E. Kristensson, M. Richter, M. Aldén, G. Göritz, K. Knebel, Ultra-high-speed pumping of an optical parametric oscillator (OPO) for high-speed laser-induced fluorescence measurements Meas. Sci. Technol. 20 (2009) 025306.
[33] R.W. Dibble, V. Hartmann, R.W. Schefer, W. Kollmann, Conditional sampling of velocity and scalars in turbulent flames using simultaneous LDV-Raman scattering, Exp. Fluids 5 (1987) 103-113.

[34] I.G. Shepherd, Flame surface density and burning rate in premixed turbulent flames, Symp. (Int.) Combust. 26 (1996) 373-379.
[35] J.B. Bell, M.S. Day, J.F. Grcar, M.J. Lijewski, J.F. Driscoll, S.A. Filatyev, Numerical simulation of a laboratory-scale turbulent slot flame, Proc. Comb. Inst. 31 (2007) 1299-1307.
[36] M. Zhang, J. Wang, W. Jin, Z. Huang, H. Kobayashi, L. Ma, Estimation of 3D flame surface density and global fuel consumption rate from 2D PLIF images of turbulent premixed flame, Combust. Flame 162 (2015) 2087-2097.
[37] J. O. Hinze, Turbulence, 2nd Edition, McGraw-Hill, Inc., New York, 1975.
[38] S. B. Pope, Turbulent Flows, Cambridge University Press, 2000.
[39] G.P. Smith, D.M. Golden, M. Frenklach, N.W. Moriarty, B. Eiteneer, M. Goldenberg, C.T. Bowman, R.K. Hanson, S. Song, J. William C. Gardiner, V.V. Lissianski, Z. Qin, GRI-Mech 3.0, 1999; http://www.me.berkeley.edu/gri_mech/
[40] C. Liu, B. Yan, G. Chen, X.S. Bai, Structures and burning velocity of biomass derived gas flames, Int. J. Hydrogen Energy 35 (2010) 542-555.
[41] P. Tamadonfar, O.L. Gulder, Flame brush characteristics and burning velocities of premixed turbulent methane/air Bunsen flames, Combust Flame 161 (2014) 3154-3165.
[42] B. Zhou, C. Brackmann, Q. Li, Z. Wang, P. Petersson, Z. Li, M. Aldén, X.S. Bai, Distributed reactions in highly turbulent premixed methane/air flames: Part I. Flame structure characterization, Combust. Flame 162 (2015) 2937-2953.
[43] C. Schulz, V. Sick, Tracer-LIF diagnostics: quantitative measurement of fuel concentration, temperature and fuel/air ratio in practical combustion systems, Prog. Energy Combust. Sci. 31 (2005) 75-121.
[44] M. Tanahashi, S. Taka, M. Shimura, T. Miyauchi, CH double-pulsed PLIF measurement in turbulent premixed flame, Exp. Fluids 45 (2008) 323-332.
[45] H.J. Hussein, S.P. Capp, W.K. George, Velocity measurements in a high-Reynolds-number, momentum-conserving, axisymmetric, turbulent jet, J. Fluid Mech. 258 (1994) 31-75.
[46] N.A.K. Doan, N. Swaminathan, N. Chakraborty, Multiscale analysis of turbulence-flame interaction in premixed flames, Proc. Comb. Inst. 36 (2017) in press.
[47] N. Peters, Laminar flamelet concepts in turbulent combustion, Symp. (Int.) Combust. 21 (1988) 1231-1250.
[48] Ö.L. Gülder, G.J. Smallwood, Inner cutoff scale of flame surface wrinkling in turbulent premixed flames, Combust. Flame 103 (1995) 107-114.
[49] H. Kobayashi, K. Seyama, H. Hagiwara, Y. Ogami, Burning velocity correlation of methane/air turbulent premixed flames at high pressure and high temperature, Proc Combust Inst. 30 (2005) 827-834.
[50] D. Bradley, How fast can we burn? Proc. Combust. Inst. 24 (1992) 247-262.
[51] S.S. Shy, W.J. Lin, K.Z. Peng, High-intensity turbulent premixed combustion: general correlations of turbulent burning velocities in a new cruciform burner, Proc. Combust. Inst. 28 (2001) 561-568.
[52] A.N. Lipatnikov, J. Chomiak, Turbulent flame speed and thickness: phenomenology, evaluation, and application in multi-dimensional simulations, Prog. Energy Combust. Sci. 28 (2002) 1-74.
[53] H. Wang, E.R. Hawkes, J.H. Chen, Turbulence-flame interaction in DNS of a laboratory high Karlovitz premixed turbulent jet flame, Physics of Fluids 28 (2016) 095107.